Electrochemical Applications of 2-Dimensional Nanosheets: The Effect of Nanosheet Length and Thickness

Zahra Gholamvand, David McAteer, Andrew Harvey, Claudia Backes, and Jonathan N. Coleman*

School of Physics, CRANN & AMBER Research Centres, Trinity College Dublin, Dublin 2, Ireland

*colemaj@tcd.ie

ABSTRACT: Although many electrochemical properties of 2D materials depend sensitively on the nanosheet dimensions, there are no systematic, quantitative studies which analyse the effect of nanosheet size and thickness on electrochemical parameters. Here we use size-selected WS_2 nanosheets as a model system to determine the effect of nanosheet dimensions in two representative areas – hydrogen evolution electrocatalytic electrodes and electrochemical double layer capacitor electrodes. We chose these applications as they depend on the interaction of ions with the nanosheet edge and basal plane, respectively, and so would be expected to be nanosheet-size-dependent. The data shows the catalytic current density to scale inversely with mean nanosheet length while the volumetric double layer capacitance scales inversely with mean nanosheet thickness. Both of these results are consistent with simple models allowing use to extract intrinsic quantities, namely the turnover frequency and the double layer thickness respectively.

INTRODUCTION

Over the last few years, it has become clear that nanoscience will play an important role in future technology for the generation and storage of energy.[1] Just two examples are the use of silicon nano-particles in lithium ion battery anodes[2] and the incorporation of carbon nanotubes in efficient solar thermophotovoltaic devices.[3] In the last few years, there has been a huge amount of interest in 2-dimensional (2D) nanomaterials for use in a range of applications related to energy generation and storage.[4, 5] There are many types of 2D materials with well-known examples being graphene, BN, transition metal dichalcogenides (TMDs - $MoSe_2$, WS_2 *etc*), transition metal oxides (TMOs – MnO_2, MoO_3 *etc*), layered double hydroxides ($Co(OH)_2$, $Ni(OH)_2$ *etc*) and a range of others including black phosphorous, silicene and germanane.[6-10]

These materials consist of covalently bonded monolayers which can stack *via* weak inter-sheet interactions to form layered crystals.[9, 11] In the context of energy applications, 2D nanomaterials are generally used in the form of nanosheets – tiny platelets with lateral size ranging from 10s of nm to microns and thickness of ~nm.[11] Such nanosheets generally consist of ~1-10 stacked monolayers and are usually prepared by liquid-based exfoliation or synthesis techniques.[9, 12-14] Such production methods are important, as the availability of nanosheets dispersed in a liquid allows the production of the films and coatings which are required for many energy-related applications.

To date, nanosheets have been used in many such applications, mainly in the electrochemical arena, in areas from photocatalysis[15] to proton transport membranes.[16] A range of 2D materials including graphene and MoS_2 have been used in electrochemical energy storage applications,[9, 17] typically as electrodes in batteries[18-20] and supercapacitors[21, 22]. Nanosheets have also been used to generate fuel (this can also be considered energy storage) *via* the catalysis of gas evolution reactions. For example, TMDs such as MoS_2 and WS_2 have been widely used as electrocatalysts for the hydrogen evolution reaction (HER) and water splitting.[23, 24] Similarly, a number of LDHs have been used successfully to catalyze the oxygen evolution reaction (OER).[25, 26] Alternatively, graphene and MoS_2 find applications to generate solar energy, notably by replacing platinum in catalytic counter electrodes in dye sensitized solar cells (DSSCs).[27, 28]

However, one basic factor that has not been comprehensively or quantitatively explored is how the performance of nanosheet-containing electrodes depends on the geometry of the nanosheets within. Nanosheet size is known to strongly affect properties such as

amphiphilicity[29] and optical behaviour[30, 31] simply because of the relationships between sheet dimensions and parameters such as the fraction of edge atoms. As such, we expect nanosheet geometry to be a critical factor in all the applications described above. This is due to the specific roles nanosheets play in electrochemical devices which tend to involve either reactions or adsorption of species which preferentially occur at specific sites on the nanosheet. We can crudely divide these into two classes of events: those which occur at the nanosheet edge and those which occur at the basal plane. In either case, the electrode performance can be enhanced by tuning the nanosheet geometry to increase the number of active sites, *i.e.* either by increasing the total perimeter length or the total accessible surface area within the electrode. Examples of processes where nanosheet edge sites are important include catalysis of the HER[32] and the tri-iodide reaction in DSSCs[27, 28] while interaction sites on the basal plane are involved for supercapacitor[33] and battery electrodes[19] as well as electrocatalysis involving the metallic 1T form of WS_2.[34, 35]

We can examine the use of TMDs to catalyse the HER as an example of a process where edge sites are important. In HER, electrons from the external circuit combine with protons from an electrolyte at a catalytic site resulting in the formation of H_2 molecules. For the semiconducting 2H polytype of many TMDs, it is known that the catalytic active sites reside on the nanosheet edge[36-41] and are probably terminal disulphide groups.[38, 41, 42] Because laterally smaller nanosheets have a greater edge length per volume, changing nanosheet size has a significant impact on catalytic activity. For example, both Wang[43] *et al.* and Benson[32] *et al.* reported using MoS_2 nanosheets of different sizes to catalyse the HER. They found improvements in both exchange current density and Tafel slope as the nanosheet size was reduced. However, they did not quantitatively analyze the dependence of either parameter on size. Very recently, we published a simple theoretical model which predicts that for edge-active nanosheet catalysts, the gas evolution rate should scale inversely with nanosheet length.[44] However, this model has not yet been tested experimentally.

Alternatively, supercapacitor electrodes fabricated from nanosheets are a good example of an electrochemical application which involves interactions which are localised at the basal plane. In a supercapacitor electrode, charge is stored at an electrode/electrolyte interface with the close proximity between charges in the electrode and ions in the electrolyte resulting in large storage capacity.[45] Supercapacitors can be either electric double layer capacitors (EDLC) where the energy is stored electrostatically or pseudocapacitors where the charge storage process involves redox reactions between ions and electrode.[45] However, in both cases, when

the electrode consists of a nanosheet network, the charge is predominately stored at the nanosheet basal plane.[33, 46] This means that the capacitance, and so the achievable energy density, can be increased by increasing the total accessible surface area within the electrode.[47] In principle, this can be done by reducing the thickness of the nanosheets. However, to our knowledge, no papers have appeared which explicitly plot capacitance versus nanosheet thickness to quantitatively analyse this behaviour.

Part of the reason why the effect of nanosheet geometry has not been quantitatively characterised for either edge or basal-plane sensitive processes is the difficulty of first controlling nanosheet dimensions and then accurately measuring either nanosheet thickness or lateral size. Without the ability to achieve both these tasks, quantifying the geometrical effects is very difficult. However, recently, advances[31, 48] in the processing and characterising of nanosheets produced by liquid phase exfoliation (LPE) has made both these tasks more straightforward.

LPE is a simple, scalable process which can be used to exfoliate layered crystals by sonication or shearing to give large quantities of nanosheets stabilised in certain liquids.[13, 49, 50] Recently, we have developed methods to routinely select nanosheets by size.[31, 48] In particularly, liquid cascade centrifugation (LCC) is a centrifugation-based sorting procedure which can effectively separate large, thick nanosheets from small, thin ones.[31] A significant advantage of this method over other sorting techniques is that very little material is lost during processing, making it ideal for preparing samples for applications. In addition, we have also developed methods to measure both lateral size and thickness of liquid-dispersed MoS_2 and WS_2 nanosheets *in-situ* using optical spectroscopy.[31, 48] The combination of both these advances will allow us to prepare sets of nanosheet dispersions with a range of accurately known thickness and lengths.

Here we use WS_2 nanosheets as a model system to study the dependence of the electrochemical properties of films of nanosheets on nanosheet dimensions. We demonstrate the production of a range of fractions of dispersed WS_2 nanosheets with a set of known mean lengths and thicknesses. These have been fabricated into films which have been studied as both electrocatalysts for HER and electrochemical double layer capacitor (EDLC) electrodes. We find the HER exchange current density to scale inversely with nanosheet length, as expected for edge sites, while the volumetric capacitance scales inversely with thickness, as expected for a process involving the basal plane. Analysing this data using simple models allows the extraction of fundamental parameters describing both processes.

RESULTS AND DISCUSSION

Characterisation of size selected nanosheets

To assess the effect of WS_2 nanosheet size on the electrochemical properties of nanosheet networks requires sets of nanosheets with controlled lateral size (*i.e.* nanosheet length, *L* defined as the longest dimension of the individual nanosheet) and thickness (*i.e.* number of monolayers per nanosheet, *N*). We achieve this using liquid cascade centrifugation (LCC), a method which is useful as it allows us to produce sets of samples with varying <*L*> for HER experiments and varying <*N*> for EDLC tests.

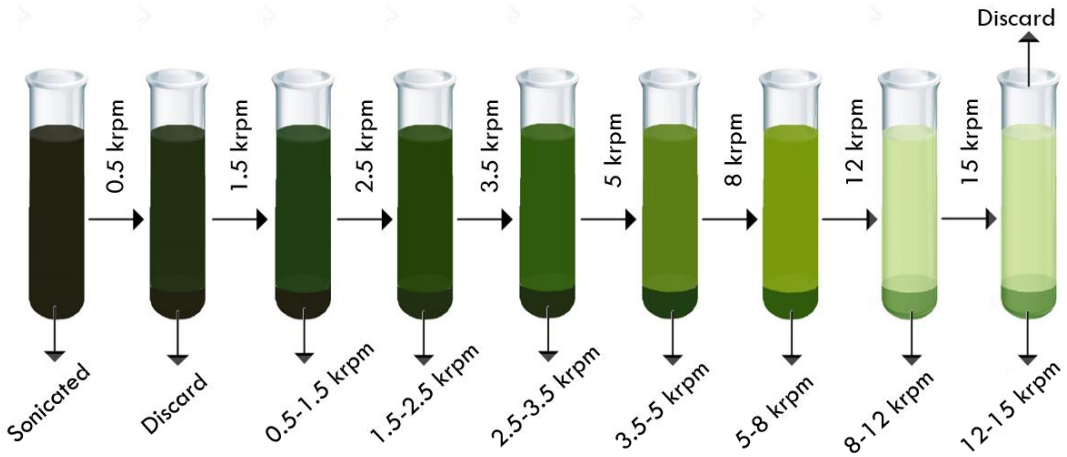

Figure 1: Schematic showing size selection by liquid cascade centrifugation with the rpm iterations used in this study. Corresponding g-forces are tabulated in Table S1. Size-selected dispersions were prepared by re-dispersing the collected sediments in 3 g/L aqueous sodium cholate.

The WS_2 dispersion with which we begin was obtained by sonication of WS_2 powder in aqueous surfactant solution (see methods) followed by low speed centrifugation (500 rpm) to remove any unexfoliated crystallites. This stock could then be size-selected using LCC.[31] The stock was first centrifuged at a relatively low speed (1500 rpm), thus separating the largest nanosheets into the sediment, leaving all others in the supernatant. These large nanosheets can then be collected in the sediment and redispersed by addition of surfactant solution followed by mild sonication. The supernatant can then be centrifuged again at a slightly higher speed with the largest remaining nanosheets being transferred to the sediment. This procedure can be repeated a number of times with the size of the nanosheets in the sediment steadily falling with

each iteration. Because each sediment is "trapped" between two slightly different centrifugation speeds, the samples are labelled according to the speeds. Hence a "1.5-2.5 krpm" sample contains larger nanosheets than a "5-8 krpm" sample. This process is illustrated in figure 1.

Here, we performed a 7-iteration LCC cascade, collecting 7 dispersions which we expect to contain nanosheets of different mean sizes. The easiest way to confirm this is *via* UV-vis extinction spectroscopy. Recently we showed that the optical extinction spectra of nanosheet dispersions depend sensitively on mean nanosheet size and thickness (extinction is defined *via* $Ext(\lambda) = -\log T(\lambda)$).[31, 48] Due to edge effects, the spectral shape (as quantified for example by $Ext_{235nm} / Ext_{290nm}$) scales with mean nanosheet length, while confinement effects shift the wavelength associated with the A-exciton with mean nanosheet thickness (see SI methods and ref [31, 48]). Shown in figure 2A and S1 are extinction spectra for a subset of the WS_2 nanosheet dispersions produced by LCC. While the general form of these spectra is as expected for the 2H polytype of WS_2,[51] it is immediately clear that both the spectral shape (and so nanosheet length) and the A-exciton position (and so nanosheet thickness) change significantly from sample to sample.

To confirm these size variations, we performed statistical transmission electron microscopic (TEM) and atomic force microscopic (AFM) analysis on three of the size-selected nanosheet dispersions ("0.5-1.5 krpm", "2.5-3.5 krpm" and "8-12 krpm"). Shown in figure 2B-C are histograms for nanosheet length measured from TEM images such as those shown in the insets for two of these samples (the equivalent data for "2.5-3.5 krpm" sample is in the SI, figure S2). The difference between these samples is stark with large nanosheets ($100<L<400$ nm) in the "0.5-1.5 krpm" sample but much smaller nanosheets ($10<L<60$ nm) in the "8-12 krpm" sample. Similar data is shown in figure 2D-E (and SI figure S3), but this time representing the nanosheet thickness as measured by AFM. Here, the nanosheets in the "0.5-1.5 krpm" sample are considerably thicker than those in the "8-12 krpm" sample.

We can quantify this by plotting the mean nanosheet length, as measured by TEM (solid symbols) *versus* the median centrifugation speed used for each sample in figure 2D. Equivalent data for mean nanosheet thickness, as measured by AFM, is plotted in figure 2G (solid symbols). In addition, we used published metrics[31] to extract mean nanosheet length and thickness from the extinction spectra (see SI). These values are also plotted *versus* the median centrifugation speed in figures 1D and E respectively. We find both nanosheet length and

thickness extracted from the extinction spectra to agree well with values measured by TEM and AFM. These graphs clearly show the nanosheet dimensions to vary strongly with median centrifugation speed with <*L*> and <*N*> varying in the ranges 325-30 nm and 14-1.3 respectively.

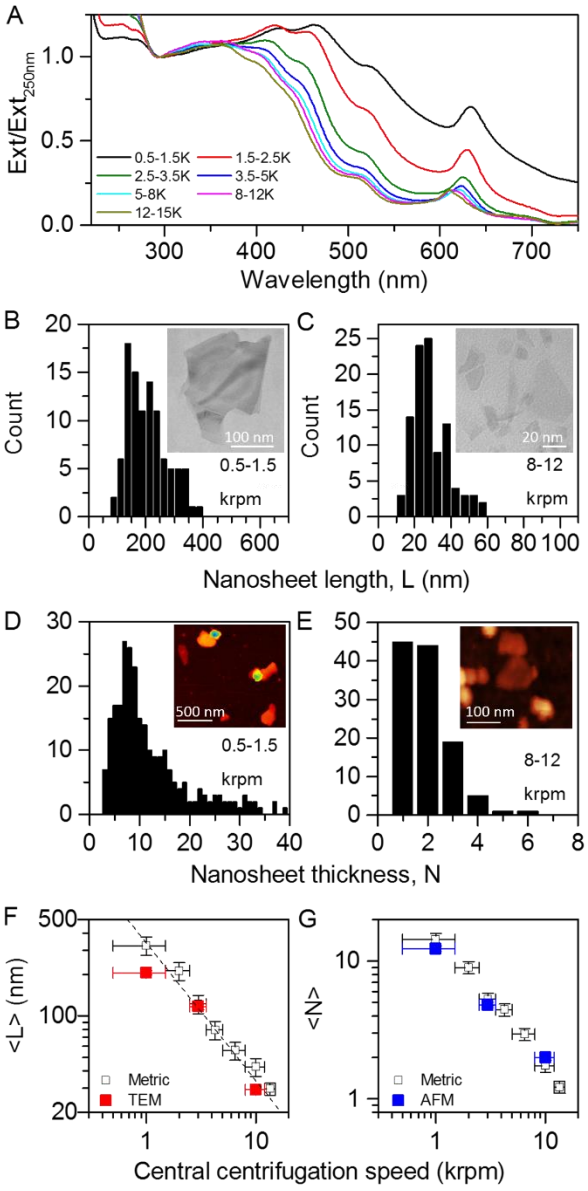

Figure 2: Basic characterisation of liquid exfoliated WS_2 nanosheets used to fabricate electrodes. A) Optical extinction spectra of dispersions prepared using different centrifugation conditions and so containing different nanosheet sizes. The mean nanosheet size can be extracted from the ratio of extinctions at 235 nm and 290 nm (Ext_{235nm} / Ext_{290nm}) while the mean nanosheet thickness can be extracted from the wavelength associated with the A-exciton (~625 nm) with details given in the SI. B-C) Histograms of nanosheet length, as measured by

TEM, for dispersions prepared using two different sets of centrifugation conditions. Shown in the insets are sample TEM images. D-E) Histograms of nanosheet thickness (number of monolayers per nanosheet, N), as measured by AFM, for dispersions prepared using two different sets of centrifugation conditions. Shown in the insets are sample AFM images. F-G) Mean nanosheet length (D) and thickness (E) plotted versus central centrifugation speed (i.e. the midpoint between upper and lower speeds used in the preparation procedure). The black, open symbols represent data extracted from extinction spectra, while the solid symbols represent average nanosheet lengths and thicknesses as measured by TEM and AFM respectively. The dashed line in D represents the expected behaviour.[31]

We have used the size-selected dispersions to prepare thin films by vacuum filtration for electrochemical investigation. Such films consist of disordered arrays of nanosheets as shown in figure 3A-B and tend to be porous (typical porosity ~50%). This is important for electrochemical applications as it allows the electrolyte access to the internal structure of the electrode. Indeed recent measurements in our group[44] on MoS_2 nanosheet networks applied as hydrogen evolution electrocatalysts showed complete catalyst penetration for electrodes of thickness up to at least 5 µm. Here, the film thicknesses were measured by profilometry (see SI methods) and ranged from 680 nm to 210 nm so we expect to whole internal surface to be exposed to electrolyte.

Dependence of HER catalysis on nanosheet size

We began by studying films of different sized WS_2 nanosheets as hydrogen evolution electrocatalysts. In its layered form, 2H-WS_2 has been known to be a catalyst for HER since at least 1988.[52] However, recently it has been shown that the efficacy of WS_2 increases dramatically once it has either been synthesised in a nanostructured form[53, 54] or when exfoliated into nanosheets.[55] During the hydrogen evolution reaction, electrons from the external circuit combine with protons at catalytic sites at the electrode/electrolyte interface resulting in the formation of H_2 gas. It has been known for some time that transition metal dichalcogenides can catalyse this reaction *via* active sites on the nanosheet edge (for the 2H-polytype).[41] Thus, as smaller nanosheets (lower $\langle L \rangle$) have more edges, they would be expected to be more effective catalysts.

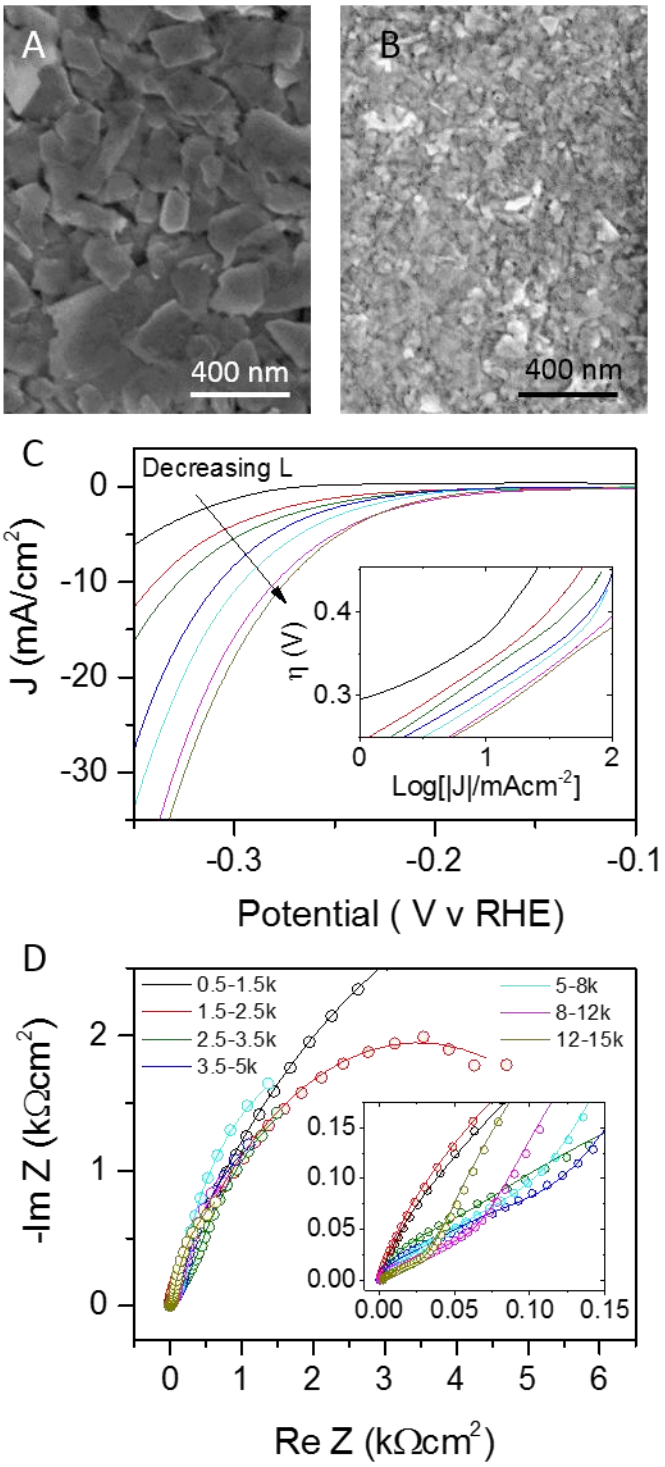

Figure 3: Characterisation of WS_2 nanosheet electrodes as catalysts for the hydrogen evolution reaction. A-B) SEM images of nanosheet films prepared using nanosheets of different sizes (mean lengths of 325 nm, sample 0.5-1.5krpm and 43 nm, sample 8-12krpm, respectively). C) Polarisation curves measured for electrodes fabricated from nanosheets of different sizes. Inset: Tafel plots. D) Nyquist plots measured at zero overpotential for the electrodes shown in

(C). The solid lines are fits to the model described in the text (see table S3 for fit parameters). The colour coding in C and D is the same, meaning the legend in D also applies to C.

We characterised the catalytic performance by measuring polarisation curves for electrodes formed from nanosheets with different <*L*> as shown in figure 3C. This data clearly demonstrates the current density and so the H_2 production rate to increase continuously as the nanosheet size falls. The inset in figure 3C shows Tafel plots (for different nanosheet size plotted as η *versus* Log|J|) which indicate the Tafel slope (measured at currents below 10 mA/cm^2) to be relatively invariant with nanosheet size. This suggests the increase in current flow to be due to changes in the number of catalytically active sites. We also measured impedance spectra at zero overpotential for all electrodes as shown in figure 3D. Here, while the changes are more subtle (see below and SI, Figure S4-S5), the Nyquist plots clearly contain more than one semicircle with the diameter of the largest semicircle changing with <*L*>. As we will demonstrate below, this indicates that the charge transfer resistance depends on nanosheet size.

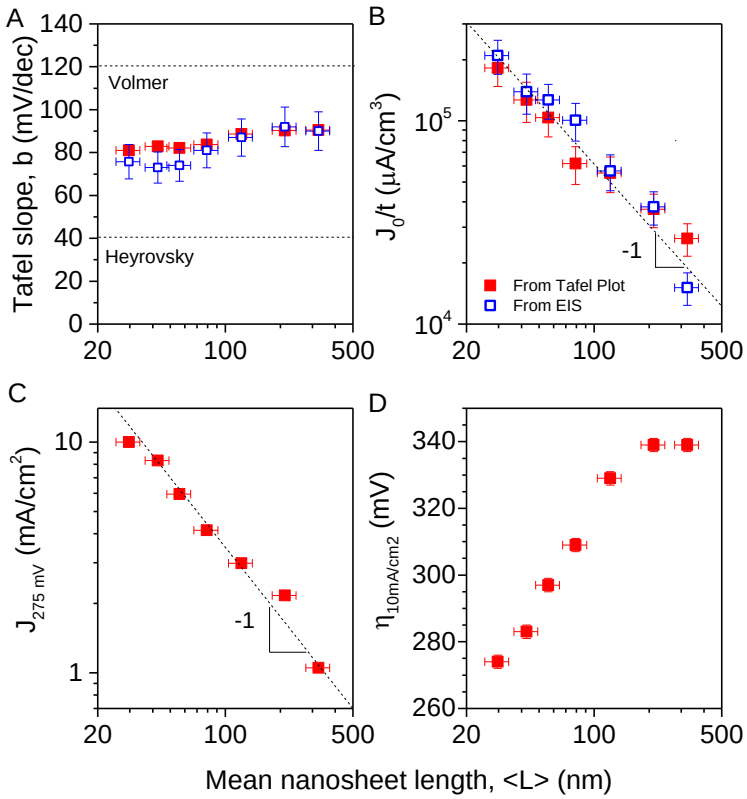

Figure 4: Analysis of the polarisation and impedance data. A) Tafel slope plotted versus mean nanosheet length, <L>. The expected Tafel slopes, if the Volmer or Heyrovsky reactions were rate limiting, are shown as dashed lines. B) Exchange current density divided by electrode thickness plotted versus <L>. Both the Tafel slope and the exchange current density were obtained in two ways: from the polarisation curves and from the Nyquist plots, as described in the text and the SI. C-D) Current density achieved at an overpotential of 275 mV (C) and overpotential required to achieve a current density of 10 mA/cm^2 (D), both plotted versus <L>.

We can analyse the polarisation data quantitatively by fitting the linear portion of the Tafel plot (*i.e.*, at currents low enough to make mass transport limitations unimportant) to the the cathodic term of the Butler-Volmer equation,[56] known as the Tafel equation, which can be written as:

$$J = -J_0 \times 10^{\eta/b} \qquad (1)$$

where J is the measured current density, J_0 is the exchange current density, η is the overpotential, and b is the Tafel slope. Extracting the Tafel slope by fitting figure 3C (inset) in the vicinity of J=10 mA/cm^2, gave values of b which are plotted *versus* <L> in figure 4A. In addition, we extracted b from impedance data as described in the SI. Both data sets were in good agreement with values in the range 70-90 mV/dec. Although the Tafel slopes are all within error of each other, there may be a weak length dependence with b increasing slightly with nanosheet length. This is broadly consistent with the results of Benson *et al.* and Wang *et al* where an increase in b was observed with increasing nanosheet size.[32, 43]

In acidic solutions, three reactions can take place when hydrogen is evolved on a catalyst surface, commonly named the Volmer, Heyrovsky and Tafel reactions with the value of b indicating the rate limiting step in the H_2 evolution process (see SI).[44] In our case, a Tafel slope of ~70-90 mV/dec is consistent with the Volmer-Heyrovsky process where proton adsorption contributes to the rate determining process.[57] This is in line with previous measurements on WS_2 which have given values of b in the range 78-110 mV/dec.[34, 53, 58-61] As indicated above, that the reaction mechanism does not change with nanosheet size indicates that the observed size dependence must be associated with changes in the number of active sites rather than the chemical nature of the active sites.

By fitting the polarization curves, we can also extract the exchange current density, J_0, in order to investigate its dependence on nanosheet size. However, care must be taken, as it is known that J_0 scales linearly with electrode thickness, t, as thicker electrodes contain more active sites.[44] Thus, we plot J_0/t versus $\langle L \rangle$ in figure 4B (closed symbols) finding a well-defined inverse dependence over almost a decade of both J_0/t and $\langle L \rangle$.

We can confirm this inverse behavior by fitting the impedance spectra shown in figure 3D to the circuit model outlined in the SI (see table S3 for fit parameters). This gives the charge transfer resistance measured at zero overpotential, $R_{ct}(\eta = 0)$, which we find decreases from 12.3 kΩcm^2 to 2.6 kΩcm^2 as $\langle L \rangle$ falls from 325 to 40 nm (*N.B.*, here we have normalized by multiplying by electrode area, A, to give $R_{ct}A$). This decrease in charge transfer resistance is due to the greater number of active edge sites present for the samples fabricated from smaller nanosheets. When measured at zero overpotential (as was the case here), R_{ct} is directly related to the exchange current density by:[62]

$$R_{ct}A = RT / nFJ_0 \qquad (2)$$

where F is Faraday's constant and n=2 is the number of electrons supplied per H_2 molecule formed. We can use this equation to calculate J_0 from the R_{ct} data extracted from fitting of impedance data. This data is also plotted as J_0/t *versus* $\langle L \rangle$ in figure 4B (open symbols) and also shows inverse behavior, agreeing very well with the data extracted from polarization curves.

This inverse dependence of J_0/t with $\langle L \rangle$ is very important, as it is exactly what would be expected if the catalytic sites reside on the nanosheet edge. For fixed length/width aspect ratio nanosheets, the monolayer edge perimeter is $\propto L$ while the monolayer volume is $\propto L^2$. Thus, the total edge length of all nanosheet layers (including edges associated with individual layers stacked in few-layer nanosheets) per unit volume scales as $\propto 1/L$. Then, if the exchange current per unit volume (*i.e.* the exchange current density per unit electrode thickness) is proportional to the number of catalytic sites per volume, we expect $J_0 / t \propto 1/\langle L \rangle$, as observed.

We can see this more formally using an equation derived recently to describe the exchange current density for catalytic electrodes consisting of porous films of edge-active nanosheets:[44]

$$J_0 = 2ne[R_0 B]\left[\frac{(1+k)(1-P)}{\langle L\rangle d_0}\right]t \qquad (3)$$

In this expression n=2 is the number of electrons supplied per H_2 molecule formed, R_0 is the zero-overpotential turnover frequency (per site), B is the number of catalytic active sites per unit nanosheet edge length, k is the nanosheet length/width aspect ratio, P is the electrode porosity, $\langle L\rangle$ is the mean nanosheet length, d_0 is the monolayer thickness and t is the electrode thickness. Here the product R_0B is the number of H_2 molecules produced per second per unit edge length (including edges associated with all individual layers stacked in few-layer nanosheets) and can be thought of as a figure of merit for the catalytic activity of a nanosheet. Equation 3 clearly has the expected form, consistent with $J_0/t \propto 1/\langle L\rangle$ allowing us to use it to extract R_0B from the data in figure 4B. The dashed line in figure 4b is a fit to equation 3 and is consistent with $d(J_0/t)/d(1/\langle L\rangle)$ =(6.1±0.5)×10^{-3} A/m^2. Taking[44] k=2 and P=0.5 gives R_0B =3.8±0.4 H_2 molecules $s^{-1}\mu m^{-1}$. This value compares with $R_0B \approx 11\pm2.5$ H_2 molecules s^{-1} μm^{-1}, estimated recently for LPE MoS_2 electrodes.[44] We note that if all edge disulphides were active,[44] then the maximum possible value of B would be 1.56 nm^{-1}, leading to a minimum value of R_0=2.4×10^{-3} s^{-1}. This can be compared with Jaramillo's value of R_0=20×10^{-3} s^{-1}, measured for MoS_2.[41] We suggest the discrepancy is either because all of the edge sites are not active in our case, perhaps due to functionalisation or breaking of the disulphide bridges during sonication, or perhaps because the intrinsic value of R_0 is smaller for 2H-WS_2 compared to 2H-MoS_2.

However, one problem with LCC is that it gives fractions where both $\langle L\rangle$ and $\langle N\rangle$ vary with iteration such that $\langle L\rangle \propto \langle N\rangle$. Thus, for the data presented in figure 4B, not only is $\langle L\rangle$ changing but so is $\langle N\rangle$. This is an important point as, while the catalytic sites reside on the nanosheet edge for 2H-TMDs, for the 1T polytype, the HER catalytic sites lie on the basal plane.[34, 35] Thus, it is important to show that the increase in current density with decreasing nanosheet size is due to increases in edge length (*i.e.* $J_0/t \propto 1/\langle L\rangle$) rather than increases in accessible surface area (which would mean $J_0/t \propto 1/\langle N\rangle$, see SI). To show this, we have derived an expression, analogous to equation 3, for the exchange current density when the active sites are on the nanosheet basal plane (see SI, equation S11). By analyzing the data in this context, we find a value of R_0 which is unrealistically small for WS_2. This shows that our data is consistent with the active sites lying on the nanosheet edge - as we would expect for

2H-WS_2. It is worth noting that equation S11 may be useful in its own right for analyzing HER catalytic data for 1T-TMDs where the catalytic sites are known to lie in the basal plane.

In practical terms, we can also characterise the performance of a hydrogen evolution electrocatalytic electrode *via* the H_2 production rate, as represented by the current density at a given potential. Shown in figure 4C is the current density at a potential of 275 mV *vs* RHE, J_{275mV}, plotted *versus* $\langle L \rangle$. This parameter falls inversely with $\langle L \rangle$ as would be expected from equations 1 and 3 (given that *b* is roughly constant). This means that a 10-fold reduction in nanosheet size results in a 10-fold current increase, highlighting the importance of size minimisation for catalytic applications. Of greater practical importance is the overpotential required to achieve a given current density. Commercial electrolyzers generally operate at fixed current density.[63] Because the power consumption of an electrolyzer is related to $J\eta$, and because the H_2 production rate is proportional to *J*, the overpotential required to generate 10 mA/cm^2 can provide an insight to the energy required to produce each H_2 molecule. This makes it very important to reduce the operating overpotential. Shown in figure 4D is the overpotential required to produce a current density of 10 mA/cm^2, $\eta_{10mA/cm2}$. This parameter falls logarithmically with decreasing nanosheet length as would be expected from equations 1 and 3. A 10-fold reduction on $\langle L \rangle$ results in a ~20% reduction in operating overpotential, a small but non-trivial reduction.

Dependence of double layer capacitance on nanosheet size

Another electrochemical application, where nanosheets are widely used is as electrodes in supercapacitors. In devices, pseudocapacitive nanosheets, such as $Ni(OH)_2$, are generally used.[64, 65] However, exfoliated TMDs have been employed as Electrical Double Layer Capacitor (EDLC) electrodes. While the 1T-polytype[33] of MoS_2 has demonstrated high capacitance, electrodes made from the 2H-polytype of a number of TMDs have shown lower performances.[66-70] Because the aim of this work is not to demonstrate high-performance supercapacitors but to explore the effect of nanosheet dimensions on the performance of supercapacitor electrodes, we have opted to use size-selected 2H-WS_2 nanosheets as a model system.

An EDLC stores energy by localising non-Faradic charges at an electrode-electrolyte interface. As the maximum stored energy density is proportional to the total accessible surface area per electrode volume,[47] porous, high surface area electrodes are often used. Porous nanosheet networks have many advantages for use as supercapacitor electrodes. For a network

of nanosheets, the capacitance can be increased by maximising the total accessible nanosheet surface area. This area will depend strongly on the nanosheet dimensions. Unless the scan rate is extremely low, it is unlikely that ions can intercalate between the individual layers of a given nanosheet. Thus the accessible surface area, A_T, can be approximated by the sum of top and bottom surfaces for all nanosheets within the electrode; $A_T = 2A_{NS}N_{NS}$, where A_{NS} is the mean nanosheet top (or bottom) surface area and N_{NS} is the number of nanosheets in the electrode. This latter parameter is just the ratio of electrode mass to mean nanosheet mass, giving:

$$A_T = \frac{2\rho_f At}{\rho_{NS} d_0 \langle N \rangle} \tag{4}$$

where ρ_f and ρ_{NS} are the film and nanosheet densities respectively, A is the geometric film area, and t, d_0 and $\langle N \rangle$ have the same meaning as above. For a non-Faradaic electrical double layer capacitor, the capacitance is given by $C = \varepsilon_r \varepsilon_0 A_T / \lambda$, where ε_r is the relative permittivity associated with the double layer region and λ is the double layer thickness.[45] Combining these equations and noting that the porosity is defined as $(1-P) = \rho_f / \rho_{NS}$, gives an expression for the capacitance per electrode volume:

$$C_V = \frac{2\varepsilon_r \varepsilon_0 (1-P)}{\lambda \langle N \rangle d_0} \tag{5}$$

This expression clearly shows that the volumetric capacitance should scale inversely with the mean nanosheet thickness.

To test this, we prepared EDLC electrodes using the same films which were used to produce the HER catalytic electrodes described above. The only difference was that the EDLC electrodes were approximately 20 times larger in area than the catalytic electrodes to reduce noise and error. We characterised these electrodes by cyclic voltammetry (CV) with all electrodes scanned at various scan rates ranging from 5 to 5000 mV/s in a limited potential window (0.1 to 0.3 V vs. RHE) where the CVs are reasonably box-like (see methods). Shown in figure 5A (see methods for details) are representative CV curves (dV/dt=25 mV/s) for electrodes prepared from three different size nanosheets (all data is shown in the SI, Figures S6). These CVs shows that, at fixed scan rate, the current flowing (*i.e.* stored charge) clearly depends on the nanosheet dimensions. To analyse this data quantitatively, we extracted the average of the magnitude of the cathodic and anodic currents at V=0.2 V *vs*. RHE (which we refer to as $J_{A/C}$, see figure 5A) for each sample at every scan rate. Because we expect the current

density to scale with electrode thickness, we plot the current as $J_{A/C}/t$ *versus* scan rate in figure 5B (all data is shown in figure S7). In all cases we find a linear behaviour at low scan rate. At higher scan rates the current begins to saturate due to either limitations associated with diffusions of ions[45, 71] or the resistance of the electrode.[72] This graph shows clearly that electrodes made from smaller nanosheets result in higher currents.

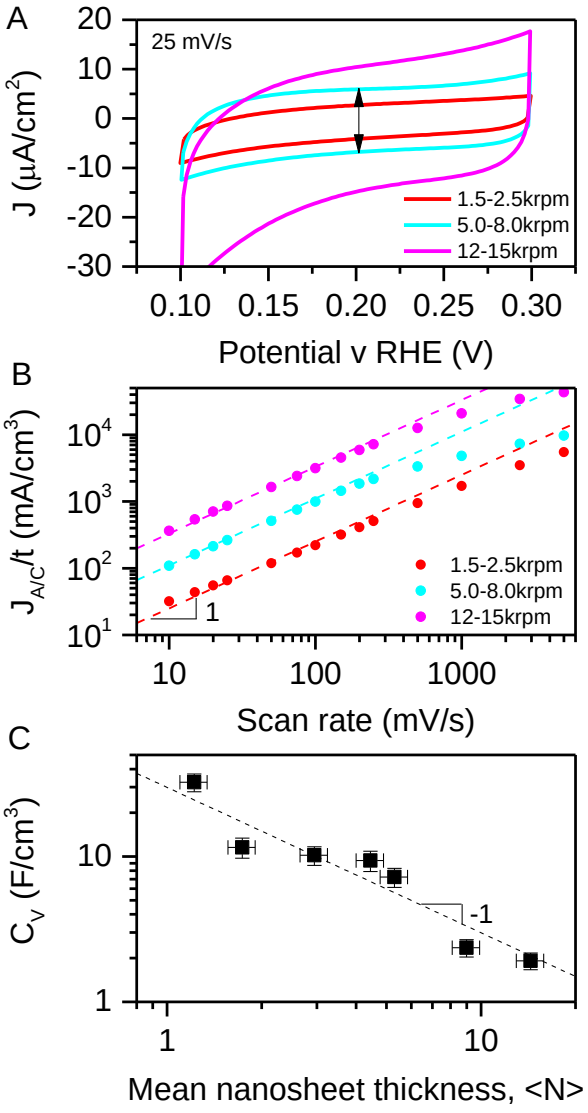

Figure 5: Characterisation of films of WS_2 nanosheets used as electrochemical double layer capacitors. A) Cyclic voltammograms (dV/dt=25 mV/s) measured for electrodes fabricated from nanosheets of different sizes. The arrow indicates $2J_{A/C}$. B) Current density, $J_{A/C}$, (measured at 0.2 V) normalised to electrode thickness plotted versus scan rate for electrodes

of three different nanosheet thickness. C) Volumetric capacitance plotted versus mean nanosheet thickness with data from all samples included.

The volumetric capacitance, C_V, of the electrodes can be found from the equation:

$$\frac{J_{A/C}}{t} = C_V \frac{dV}{dt} \quad (6)$$

We extracted C_V from the linear portion of curves such as those in figure 5B, plotting the resultant data for the volumetric capacitance versus $\langle N \rangle$ in figure 5C. Although some scatter is present, we find a clear inverse dependence of C_V with $\langle N \rangle$ as predicted by equation 5. The dashed line shows a fit to equation 5 which is consistent with $dC_V / d(1/\langle N \rangle) = (3.0 \pm 0.5) \times 10^7$ F/m^3. Taking P=0.5 and $\varepsilon_r \approx 10$,(ref [45]) we can use equation 5 to estimate that λ=5±1 nm.

This value of λ is somewhat larger than the expected value of ~1 nm,[45, 47] implying that the measured capacitances are smaller than expected for the measured nanosheet thicknesses. We note that the nanosheet thicknesses were measured spectroscopically for nanosheets dispersed in liquid. It is entirely possible that some degree of aggregation occurs during film formation, resulting in somewhat increased nanosheet thicknesses, or rather decreased accessible surface area in the film compared to the liquid. Alternatively, the accessible surface area can be reduced when parts of the pore structure are not open enough to allow access to the surface.[73] This could mean that only a (size-independent) fraction of the basal plane surface area is accessible. However, the inverse dependence of C_V on $\langle N \rangle$ observed in figure 5C indicates that the either effect must occur to the same degree for all nanosheet thicknesses.

CONCLUSION

In this work, we have used liquid cascade centrifugation to prepare a set of dispersions of size-selected WS_2 nanosheets with a well-defined range of lengths and thicknesses. These have been used to explore the dependence of two well-known electrochemical applications on nanosheet dimensions. By using films of WS_2 nanosheets to catalyse the hydrogen evolution reaction, we have shown the exchange current density to vary inversely with nanosheet length. This is in line with theoretical predictions assuming catalytically active sites to reside on the nanosheet edge. Fitting the theory to the data allows us to extract a minimum value for the turnover frequency and suggests WS_2 to be an inferior HER catalyst to MoS_2. Likewise, we have used WS_2 nanosheet films as electrical double layer capacitor electrodes. We found the

volumetric capacitance to scale inversely with the mean nanosheet thickness (as measured in dispersion). Again this is consistent with a model based on the accessible surface area in the interior of the electrode. Fitting the model to the data gives a double layer thickness which is slightly larger than expected suggesting the nanosheets to have aggregated somewhat during film formation.

This work clearly shows the importance of controlling the nanosheet dimensions for applications in electrochemistry. It is likely that size effects, similar to those seen here, will be important for other applications such as battery electrodes or other types of catalysis. We believe methods such as liquid cascade centrifugation will be critical for preparing nanosheets with size which is optimised for a given application.

Methods

Preparation of WS_2 dispersion

The WS_2 dispersion was prepared by dispersing layered powder (WS_2, Sigma Aldrich, <2 μm) with an initial concentration of 20 g/L in 70 mL aqueous surfactant solution (sodium cholate SC, C_{cs}= 10 g/L). The mixture was subjected to sonication with a high power sonic probe (VibraCell CVX; 750 W, 60 kHz) with a flathead tip for 1 h at 60% amplitude (pulse rate 6 on 2 s off) while chilled using a double jacketed water cooling system and chiller. The resultant dispersion was centrifuged in 28 mL vials in Hettich Mikro 220R centrifuge equipped with a fixed-angle rotor 1016 at 5500 krpm for 90 min. The supernatant, containing very small nanoparticles and impurities, was discarded. The sediment was redispersed in the solution of 3 g/L sodium cholate to a volume of 70 mL and subjected to the second sonication for 8 h at 60% amplitude, pulse rate 6 on 2 s off to exfoliate WS_2 layered crystals. This gives a polydisperse WS_2 stock dispersion containing both un-exfoliated crystallites and exfoliated WS_2 nanosheets which will be subjected to size selection as described below.

Size selection

The size selection procedure is adopted from our previously reported liquid cascade centrifugation[31] as is illustrated in figure 1 of the main manuscript. All centrifugations were performed in a Hettich Mikro 220R benchtio centrifuge at 15°C for 90 min, Two different rotors were used. For speeds ≤ 5 krpm, a fixed angle rotor 1016 was used (28 mL vials, ~10 mL aliquots in each vial). For this centrifuge and this rotor, the centrifugation rate, *f* is related

to the centrifugal force via $RCF = 106.4\, f^2$ where f is the rotation rate in krpm. For speeds > 5 krpm, samples were centrifuged in a 1195-A fixed angle rotor (1.5 mL vials), where f is related to the centrifugal force via $RCF = 97.4\, f^2$. The following specific procedure was applied as size selection: Un-exfoliated WS_2 crystallites were removed by centrifugation at 0.5 krpm (discard the sediment in this step). The supernatant was subjected to further 90 min centrifugation at 1.5 krpm. The sediment was redispersed in the desired volume (5 to 10 mL) of fresh surfactant (C_{cs}= 3 g/L) and labelled as "Sample 0.5-1.5 krpm", while the supernatant was centrifuged at 2.5 krpm. Again, the sediment was collected (Sample 1.5-2.5 krpm) and the supernatant subjected to centrifugation at higher speeds. This procedure was repeated with the 3.5 krpm, 5 krpm, 8 krpm, and 12 krpm as illustrated schematically in figure 1. The sediments collected contained various masses of WS_2 from 181 mg for the 0.5-1.5 krpm sample to 2.5 mg for the 12-15krpm sample (see SI). The data presented in Figure 2 uses the central rpm to express the consecutive centrifugation. The related g-forces are summarised in table S1.

Electrode preparation

Dispersions of WS_2 in SC were vacuum filtered through porous mixed cellulose ester filter membranes (MF-Millipore membrane, hydrophilic, 0.025 μm pore size, D=47 mm). Control over the deposited mass per unit area (M/A) of the filtered material was achieved by filtering known volumes of a dispersion with known concentration. This resulted in spatially uniform films with targeted M/A of ~0.02 mg/cm^2 (see for example figure 3A). To remove the remaining surfactant, all the films were washed by filtering 200 mL of deionized water through the porous films. The resulting films once dried, were cut to the desired dimensions and transferred onto glassy carbon disc electrodes for electrochemical measurements or glass substrates for SEM imaging and profilometry thickness measurements. The cellulose membrane was removed by applying pressure to the film, wetting it with acetone vapour, and subjecting it to a series of acetone baths. The acetone dissolves the cellulose membrane and leaves the porous films behind on the substrate surface.

However, we note that even though we made efforts to keep the deposited mass constant, some variation in film mass is inevitable due to factors such as inaccuracies in the extinction coefficient, leakage of the dispersion during filtration or incomplete transfer. This makes it critical to measure the thickness of all electrodes after deposition. Film thicknesses were measured using a Dektak 6M profilometer from Veeco Instruments. Step profiles were taken at four different locations to get an average film thickness for each electrode. The resultant thicknesses are shown in table S2. In all cases the electrode porosities were taken as

P=0.5. We have found that in most cases, nanosheet networks have porosity close to 50% independent of nanosheet type.[44, 74, 75]

Characterization equipment

Optical extinction was measured on Varian Cary 500 in quartz cuvettes with a pathlength of 0.4 cm in 1 nm increments.

SEM images were obtained using a ZEISS Ultra Plus (Carl Zeiss Group), 2 kV accelerating voltage, and a working distance of approximately 1−2 mm. The samples were loaded onto the SEM stub using sticky carbon tape. Bright field transmission electron microscopy imaging was performed using a JEOL 2100, operated at 200 kV on holey carbon grids (400 mesh). Statistical analysis was preformed of the flake dimensions by measuring the longest axis of the nano-sheet and assigning it "length" for > 100 nanosheets. The data is presented as arithmetic mean value of the measured length.

Atomic force microscopy (AFM) was carried out on a Dimension ICON3 scanning probe microscope (Bruker AXS S.A.S.) in tapping mode in air under ambient conditions using aluminum coated silicon cantilevers (OTESP-R3). A drop of the dispersion (20 μL) was deposited on a pre-heated (150 °C) Si/SiO_2 wafer (1x1 cm^2) with an oxide layer of 300 nm. The high concentration dispersions collected after LCC were diluted with water (to optical densities at ~400 nm of 0.1-0.2) immediately prior to deposition to reduce surfactant concentrations. After deposition, the wafer was rinsed with ~5 mL of water and ~5 mL of isopropanol. Typical image sizes ranged from 2x2 μm^2 to maximum 6x6 μm^2 for the larger nanosheets at scan rates of 0.8-1.0 Hz with 512 lines per image. The apparent thickness was measured for 100-250 nanosheets per sample and converted to number of layers using previously developed step-height analysis of liquid-exfoliated TMDs.[30, 31] The data is shown as arithmetic mean of the number of layers.

Electrochemical measurements

All the electrochemical measurements were performed with a Gamry Reference 3000 potentiostat in 0.5 M H_2SO_4 solution using a three-electrode cell, with a Calomel reference electrode (Saturated KCl, E_0=240 mV *vs.* RHE) and platinum spring as counter electrode. All the measurements were carried out in oxygen-free sealed cell under purging pure nitrogen on top of the electrolyte. The measured potential was converted to the reversible hydrogen electrode (RHE) scale by adding +0.240 V, measured with respect to a Gaskatel Hydroflex H_2 reference electrode. Catalytic activity was measured by performing linear sweep voltammetry

from 0 to -0.8 V (*vs.* RHE) with a scan rate of 5 mV/s. The AC impedance is measured within the frequency range of 0.1 to 10^6 Hz with a perturbation voltage amplitude of 10 mV and under zero and different DC potential bias. The equivalent series resistance of the system was measured by impedance spectroscopy from the high frequency intercept with the real impedance axis and all the data were corrected by iR compensation. Double layer capacitance were measured by running cyclic voltammetry between 0.1 to +0.3 V *vs* RHE with 10 cycle for each scan rate for all samples (figure S6-7). This potential window was chosen to minimise the possibility of Faradaic reactions taking place such that all the capacitance could be accounted for non-faradic double layer capacitance which depends on the accessible surface area. This allows us to use equation 5 to quantitatively analyse our data. Also the electrolyte was purged thoroughly with pure nitrogen 30 min before each experiment and blown on the surface of the fully sealed electrochemical cell during the experiment to avoid any possible oxygen reduction faradic current in voltammograms. Samples were conditioned at an appropriate voltage 1 min before each measurement.

Supporting Information Available: Detailed methods, materials characterisation and characterisation. This material is available free of charge *via* the Internet at http://pubs.acs.org.

Acknowledgement

The research leading to these results was funded by Science Foundation Ireland grant number (11/PI/1087) and European Research Council (SEMANTICS). We have also received funding from the European Union Seventh Framework Program under grant agreement n°604391 Graphene Flagship and from the Science Foundation Ireland (SFI) funded centre AMBER (SFI/12/RC/2278).

References

1. Zhang, Q.; Uchaker, E.; Candelaria, S. L.; Cao, G., Nanomaterials for Energy Conversion and Storage. *Chemical Society Reviews* **2013,** 42, 3127-3171.
2. Wu, H.; Yu, G.; Pan, L.; Liu, N.; McDowell, M. T.; Bao, Z.; Cui, Y., Stable Li-Ion Battery Anodes by in-Situ Polymerization of Conducting Hydrogel to Conformally Coat Silicon Nanoparticles. *Nat Commun* **2013,** 4.
3. Lenert, A.; Bierman, D. M.; Nam, Y.; Chan, W. R.; Celanovic, I.; Soljacic, M.; Wang, E. N., A Nanophotonic Solar Thermophotovoltaic Device. *Nature Nanotechnology* **2014,** 9, 126-130.
4. Bonaccorso, F.; Colombo, L.; Yu, G.; Stoller, M.; Tozzini, V.; Ferrari, A. C.; Ruoff, R. S.; Pellegrini, V., Graphene, Related Two-Dimensional Crystals, and Hybrid Systems for Energy Conversion and Storage. *Science* **2015,** 347, 1246501.

5. Sun, Y.; Wu, Q.; Shi, G., Graphene Based New Energy Materials. *Energy & Environmental Science* **2011,** 4, 1113-1132.
6. Xu, M.; Liang, T.; Shi, M.; Chen, H., Graphene-Like Two-Dimensional Materials. *Chemical Reviews (Washington, DC, United States)* **2013,** 113, 3766-3798.
7. Nicolosi, V.; Chhowalla, M.; Kanatzidis, M. G.; Strano, M. S.; Coleman, J. N., Liquid Exfoliation of Layered Materials. *Science* **2013,** 340, 1420-+.
8. Balendhran, S.; Walia, S.; Nili, H.; Ou, J. Z.; Zhuiykov, S.; Kaner, R. B.; Sriram, S.; Bhaskaran, M.; Kalantar-zadeh, K., Two-Dimensional Molybdenum Trioxide and Dichalcogenides. *Adv. Funct. Mater.* **2013,** 23, 3952-3970.
9. Chhowalla, M.; Shin, H. S.; Eda, G.; Li, L.-J.; Loh, K. P.; Zhang, H., The Chemistry of Two-Dimensional Layered Transition Metal Dichalcogenide Nanosheets. *Nature Chemistry* **2013,** 5, 263-275.
10. Wang, Q. H.; Kalantar-Zadeh, K.; Kis, A.; Coleman, J. N.; Strano, M. S., Electronics and Optoelectronics of Two-Dimensional Transition Metal Dichalcogenides. *Nature Nanotechnology* **2012,** 7, 699-712.
11. Nicolosi, V.; Chhowalla, M.; Kanatzidis, M. G.; Strano, M. S.; Coleman, J. N., Liquid Exfoliation of Layered Materials. *Science* **2013,** 340, 122641.
12. Elías, A. L.; Perea-López, N.; Castro-Beltrán, A.; Berkdemir, A.; Lv, R.; Feng, S.; Long, A. D.; Hayashi, T.; Kim, Y. A.; Endo, M., Controlled Synthesis and Transfer of Large-Area Ws2 Sheets: From Single Layer to Few Layers. *ACS Nano* **2013,** 7, 5235-5242.
13. Coleman, J. N.; Lotya, M.; O'Neill, A.; Bergin, S. D.; King, P. J.; Khan, U.; Young, K.; Gaucher, A.; De, S.; Smith, R. J.; Shvets, I. V.; Arora, S. K.; Stanton, G.; Kim, H.-Y.; Lee, K.; Kim, G. T.; Duesberg, G. S.; Hallam, T.; Boland, J. J.; Wang, J. J.; Donegan, J. F.; Grunlan, J. C.; Moriarty, G.; Shmeliov, A.; Nicholls, R. J.; Perkins, J. M.; Grieveson, E. M.; Theuwissen, K.; McComb, D. W.; Nellist, P. D.; Nicolosi, V., Two-Dimensional Nanosheets Produced by Liquid Exfoliation of Layered Materials. *Science* **2011,** 331, 568-571.
14. Parvez, K.; Wu, Z.-S.; Li, R.; Liu, X.; Graf, R.; Feng, X.; Müllen, K., Exfoliation of Graphite into Graphene in Aqueous Solutions of Inorganic Salts. *J Am Chem Soc* **2014,** 136, 6083-6091.
15. Sang, Y. H.; Zhao, Z. H.; Zhao, M. W.; Hao, P.; Leng, Y. H.; Liu, H., From Uv to near-Infrared, Ws2 Nanosheet: A Novel Photocatalyst for Full Solar Light Spectrum Photodegradation. *Adv. Mater.* **2015,** 27, 363-369.
16. Hu, S.; Lozada-Hidalgo, M.; Wang, F. C.; Mishchenko, A.; Schedin, F.; Nair, R. R.; Hill, E. W.; Boukhvalov, D. W.; Katsnelson, M. I.; Dryfe, R. A. W.; Grigorieva, I. V.; Wu, H. A.; Geim, A. K., Proton Transport through One-Atom-Thick Crystals. *Nature* **2014,** 516, 227-230.
17. Bonaccorso, F.; Colombo, L.; Yu, G.; Stoller, M.; Tozzini, V.; Ferrari, A. C.; Ruoff, R. S.; Pellegrini, V., Graphene, Related Two-Dimensional Crystals, and Hybrid Systems for Energy Conversion and Storage. *Science* **2015,** 347.
18. Yoo, E.; Kim, J.; Hosono, E.; Zhou, H.-s.; Kudo, T.; Honma, I., Large Reversible Li Storage of Graphene Nanosheet Families for Use in Rechargeable Lithium Ion Batteries. *Nano Letters* **2008,** 8, 2277-2282.
19. Hassoun, J.; Bonaccorso, F.; Agostini, M.; Angelucci, M.; Betti, M. G.; Cingolani, R.; Gemmi, M.; Mariani, C.; Panero, S.; Pellegrini, V.; Scrosati, B., An Advanced Lithium-Ion Battery Based on a Graphene Anode and a Lithium Iron Phosphate Cathode. *Nano Letters* **2014,** 14, 4901-4906.
20. Du, G.; Guo, Z.; Wang, S.; Zeng, R.; Chen, Z.; Liu, H., Superior Stability and High Capacity of Restacked Molybdenum Disulfide as Anode Material for Lithium Ion Batteries. *Chemical Communications (Cambridge, United Kingdom)* **2010,** 46, 1106-1108.
21. Liu, C.; Yu, Z.; Neff, D.; Zhamu, A.; Jang, B. Z., Graphene-Based Supercapacitor with an Ultrahigh Energy Density. *Nano Letters* **2010,** 10, 4863-4868.
22. Higgins, T. M.; McAteer, D.; Coelho, J. C. M.; Sanchez, B. M.; Gholamvand, Z.; Moriarty, G.; McEvoy, N.; Berner, N. C.; Duesberg, G. S.; Nicolosi, V.; Coleman, J. N., Effect of Percolation on the Capacitance of Supercapacitor Electrodes Prepared from Composites of Manganese Dioxide Nanoplatelets and Carbon Nanotubes. *Acs Nano* **2014,** 8, 9567-9579.
23. Merki, D.; Hu, X., Recent Developments of Molybdenum and Tungsten Sulfides as Hydrogen Evolution Catalysts. *Energy & Environmental Science* **2011,** 4, 3878.

24. Wang, F.; Shifa, T. A.; Zhan, X.; Huang, Y.; Liu, K.; Cheng, Z.; Jiang, C.; He, J., Recent Advances in Transition-Metal Dichalcogenide Based Nanomaterials for Water Splitting. *Nanoscale* **2015,** 7, 19764-19788.
25. Liang, H.; Meng, F.; Caban-Acevedo, M.; Li, L.; Forticaux, A.; Xiu, L.; Wang, Z.; Jin, S., Hydrothermal Continuous Flow Synthesis and Exfoliation of Nico Layered Double Hydroxide Nanosheets for Enhanced Oxygen Evolution Catalysis. *Nano Letters* **2015,** 15, 1421-1427.
26. Song, F.; Hu, X., Exfoliation of Layered Double Hydroxides for Enhanced Oxygen Evolution Catalysis. *Nature Communications* **2014,** 5.
27. Zhang, D. W.; Li, X. D.; Li, H. B.; Chen, S.; Sun, Z.; Yin, X. J.; Huang, S. M., Graphene-Based Counter Electrode for Dye-Sensitized Solar Cells. *Carbon* **2011,** 49, 5382-5388.
28. Yue, G.; Lin, J.-Y.; Tai, S.-Y.; Xiao, Y.; Wu, J., A Catalytic Composite Film of Mos2/Graphene Flake as a Counter Electrode for Pt-Free Dye-Sensitized Solar Cells. *Electrochimica Acta* **2012,** 85, 162-168.
29. Cote, L. J.; Kim, J.; Tung, V. C.; Luo, J. Y.; Kim, F.; Huang, J. X., Graphene Oxide as Surfactant Sheets. *Pure Appl. Chem.* **2011,** 83, 95-110.
30. Backes, C.; Smith, R. J.; McEvoy, N.; Berner, N. C.; McCloskey, D.; Nerl, H. C.; O'Neill, A.; King, P. J.; Higgins, T.; Hanlon, D.; Scheuschner, N.; Maultzsch, J.; Houben, L.; Duesberg, G. S.; Donegan, J. F.; Nicolosi, V.; Coleman, J. N., Edge and Confinement Effects Allow in Situ Measurement of Size and Thickness of Liquid-Exfoliated Nanosheets. *Nat Commun* **2014,** 5, 4576.
31. Backes, C.; Szydłowska, B. M.; Harvey, A.; Yuan, S.; Vega-Mayoral, V.; Davies, B. R.; Zhao, P.-l.; Hanlon, D.; Elton J. G. Santos; Katsnelson, M. I.; Blau, W. J.; Gadermaie, C.; Coleman, J. N., Production of Highly Monolayer Enriched Dispersions of Liquid-Exfoliated Nanosheets by Liquid Cascade Centrifugation. *ACS Nano* **2016,** 10, 1589–1601.
32. Benson, J.; Li, M.; Wang, S.; Wang, P.; Papakonstantinou, P., Electrocatalytic Hydrogen Evolution Reaction on Edges of a Few Layer Molybdenum Disulfide Nanodots. *ACS Appl Mater Interfaces* **2015,** 7, 14113-22.
33. Acerce, M.; Voiry, D.; Chhowalla, M., Metallic 1t Phase Mos2 Nanosheets as Supercapacitor Electrode Materials. *Nature Nanotechnology* **2015,** 10, 313-318.
34. Lukowski, M. A.; Daniel, A. S.; English, C. R.; Meng, F.; Forticaux, A.; Hamers, R. J.; Jin, S., Highly Active Hydrogen Evolution Catalysis from Metallic Ws 2 Nanosheets. *Energy & Environmental Science* **2014,** 7, 2608-2613.
35. Voiry, D.; Salehi, M.; Silva, R.; Fujita, T.; Chen, M.; Asefa, T.; Shenoy, V. B.; Eda, G.; Chhowalla, M., Conducting Mos(2) Nanosheets as Catalysts for Hydrogen Evolution Reaction. *Nano Lett* **2013,** 13, 6222-7.
36. Chou, S. S.; Sai, N.; Lu, P.; Coker, E. N.; Liu, S.; Artyushkova, K.; Luk, T. S.; Kaehr, B.; Brinker, C. J., Understanding Catalysis in a Multiphasic Two-Dimensional Transition Metal Dichalcogenide. *Nature Communications* **2015,** 6.
37. Asadi, M.; Kumar, B.; Behranginia, A.; Rosen, B. A.; Baskin, A.; Repnin, N.; Pisasale, D.; Phillips, P.; Zhu, W.; Haasch, R., Robust Carbon Dioxide Reduction on Molybdenum Disulphide Edges. *Nature Communications* **2014,** 5, 4470.
38. Hinnemann, B.; Moses, P. G.; Bonde, J.; Jørgensen, K. P.; Nielsen, J. H.; Horch, S.; Chorkendorff, I.; Nørskov, J. K., Biomimetic Hydrogen Evolution: Mos2 Nanoparticles as Catalyst for Hydrogen Evolution. *J Am Chem Soc* **2005,** 127, 5308-5309.
39. Chhowalla, M.; Shin, H. S.; Eda, G.; Li, L.-J.; Loh, K. P.; Zhang, H., The Chemistry of Two-Dimensional Layered Transition Metal Dichalcogenide Nanosheets. *Nat Chem* **2013,** 5, 263-275.
40. Tsai, C.; Chan, K.; Abild-Pedersen, F.; Norskov, J. K., Active Edge Sites in Mose2 and Wse2 Catalysts for the Hydrogen Evolution Reaction: A Density Functional Study. *Physical Chemistry Chemical Physics* **2014,** 16, 13156-13164.
41. Jaramillo, T. F.; Jorgensen, K. P.; Bonde, J.; Nielsen, J. H.; Horch, S.; Chorkendorff, I., Identification of Active Edge Sites for Electrochemical H2 Evolution from Mos2 Nanocatalysts. *Science* **2007,** 317, 100-102.
42. Lassalle-Kaiser, B.; Merki, D.; Vrubel, H.; Gul, S.; Yachandra, V. K.; Hu, X. L.; Yano, J., Evidence from in Situ X-Ray Absorption Spectroscopy for the Involvement of Terminal Disulfide in the Reduction of Protons by an Amorphous Molybdenum Sulfide Electrocatalyst. *J Am Chem Soc* **2015,** 137, 314-321.

43. Wang, T.; Gao, D.; Zhuo, J.; Zhu, Z.; Papakonstantinou, P.; Li, Y.; Li, M., Size-Dependent Enhancement of Electrocatalytic Oxygen-Reduction and Hydrogen-Evolution Performance of Mos2 Particles. *Chemistry-A European Journal* **2013,** 19, 11939-11948.
44. McAteer, D.; Gholamvand, Z.; McEvoy, N.; Harvey, A.; O'Malley, E.; Duesberg, G. S.; Coleman, J. N., Thickness Dependence and Percolation Scaling of Hydrogen Production Rate in Mos2 Nanosheet and Nanosheet-Carbon Nanotube Composite Catalytic Electrodes *ACS Nano, ASAP* **2015,** DOI:10.1021/acsnano.5b05907.
45. Conway, B. E., *Electrochemical Supercapacitors Scientific Fundamentals and Technological Applications*. Springer US: 1999.
46. Zhu, Y.; Cao, C.; Tao, S.; Chu, W.; Wu, Z.; Li, Y., Ultrathin Nickel Hydroxide and Oxide Nanosheets: Synthesis, Characterizations and Excellent Supercapacitor Performances. *Scientific Reports* **2014,** 4.
47. Béguin, F.; Frackowiak, E., *Carbons for Electrochemical Energy Storage and Conversion Systems*. CRC Press: 2010.
48. Backes, C.; Smith, R. J.; McEvoy, N.; Berner, N. C.; McCloskey, D.; Nerl, H. C.; O'Neill, A.; King, P. J.; Higgins, T.; Hanlon, D.; Scheuschner, N.; Maultzsch, J.; Houben, L.; Duesberg, G. S.; Donegan, J. F.; Nicolosi, V.; Coleman, J. N., Edge and Confinement Effects Allow in Situ Measurement of Size and Thickness of Liquid-Exfoliated Nanosheets. *Nature Communications* **2014,** 5, 4576.
49. Hernandez, Y.; Nicolosi, V.; Lotya, M.; Blighe, F. M.; Sun, Z.; De, S.; McGovern, I. T.; Holland, B.; Byrne, M.; Gun'ko, Y. K.; Boland, J. J.; Niraj, P.; Duesberg, G.; Krishnamurthy, S.; Goodhue, R.; Hutchison, J.; Scardaci, V.; Ferrari, A. C.; Coleman, J. N., High-Yield Production of Graphene by Liquid-Phase Exfoliation of Graphite. *Nature Nanotechnology* **2008,** 3, 563-568.
50. Paton, K. R.; Varrla, E.; Backes, C.; Smith, R. J.; Khan, U.; O'Neill, A.; Boland, C.; Lotya, M.; Istrate, O. M.; King, P.; Higgins, T.; Barwich, S.; May, P.; Puczkarski, P.; Ahmed, I.; Moebius, M.; Pettersson, H.; Long, E.; Coelho, J.; O'Brien, S. E.; McGuire, E. K.; Sanchez, B. M.; Duesberg, G. S.; McEvoy, N.; Pennycook, T. J.; Downing, C.; Crossley, A.; Nicolosi, V.; Coleman, J. N., Scalable Production of Large Quantities of Defect-Free Few-Layer Graphene by Shear Exfoliation in Liquids. *Nat Mater* **2014,** 13, 624-630.
51. Wilson, J. A.; Yoffe, A. D., Transition Metal Dichalcogenides Discussion and Interpretation of Observed Optical, Electrical and Structural Properties. *Advances in Physics* **1969,** 18, 193-&.
52. Sobczynski, A.; Yildiz, A.; Bard, A. J.; Campion, A.; Fox, M. A.; Mallouk, T.; Webber, S. E.; White, J. M., Tungsten Disulfide: A Novel Hydrogen Evolution Catalyst for Water Decomposition. *The Journal of Physical Chemistry* **1988,** 92, 2311-2315.
53. Zhang, Y.; Shi, J.; Han, G.; Li, M.; Ji, Q.; Ma, D.; Zhang, Y.; Li, C.; Lang, X.; Zhang, Y., Chemical Vapor Deposition of Monolayer Ws2 Nanosheets on Au Foils toward Direct Application in Hydrogen Evolution. *Nano research* **2015,** 8, 2881-2890.
54. Bonde, J.; Moses, P. G.; Jaramillo, T. F.; Norskov, J. K.; Chorkendorff, I., Hydrogen Evolution on Nano-Particulate Transition Metal Sulfides. *Faraday Discussions* **2009,** 140, 219-231.
55. Cheng, L.; Huang, W.; Gong, Q.; Liu, C.; Liu, Z.; Li, Y.; Dai, H., Ultrathin Ws_2 Nanoflakes as a High-Performance Electrocatalyst for the Hydrogen Evolution Reaction. *Angewandte Chemie* **2014,** 126, 7994-7997.
56. Atkins, P.; de Paula, J., *Physical Chemistry*. W. H. Freeman: 2009.
57. Conway, B.; Tilak, B., Interfacial Processes Involving Electrocatalytic Evolution and Oxidation of H 2, and the Role of Chemisorbed H. *Electrochimica Acta* **2002,** 47, 3571-3594.
58. Ambrosi, A.; Sofer, Z.; Pumera, M., 2h -> 1t Phase Transition and Hydrogen Evolution Activity of Mos2, Mose2, Ws2 and Wse2 Strongly Depends on the Mx2 Composition. *Chemical Communications (Cambridge, United Kingdom)* **2015,** 51, 8450-8453.
59. Chia, X.; Ambrosi, A.; Sofer, Z.; Luxa, J.; Pumera, M., Catalytic and Charge Transfer Properties of Transition Metal Dichalcogenides Arising from Electrochemical Pretreatment. *ACS Nano* **2015,** 9, 5164-5179.
60. Pu, Z.; Liu, Q.; Asiri, A. M.; Obaid, A. Y.; Sun, X., One-Step Electrodeposition Fabrication of Graphene Film-Confined Ws2 Nanoparticles with Enhanced Electrochemical Catalytic Activity for Hydrogen Evolution. *Electrochimica Acta* **2014,** 134, 8-12.

61. Voiry, D.; Yamaguchi, H.; Li, J. W.; Silva, R.; Alves, D. C. B.; Fujita, T.; Chen, M. W.; Asefa, T.; Shenoy, V. B.; Eda, G.; Chhowalla, M., Enhanced Catalytic Activity in Strained Chemically Exfoliated Ws_2 Nanosheets for Hydrogen Evolution. *Nat Mater* **2013,** 12, 850-855.
62. Jerkiewicz, G.; Feliu-Martinez, J.; Popov, B. N., *Hydrogen at Surface and Interfaces: Proceedings of the International Symposium*. The Electrochemical Society: 2000.
63. Carmo, M.; Fritz, D. L.; Mergel, J.; Stolten, D., A Comprehensive Review on Pem Water Electrolysis. *International Journal of Hydrogen Energy* **2013,** 38, 4901-4934.
64. Chen, H.; Hu, L.; Yan, Y.; Che, R.; Chen, M.; Wu, L., One-Step Fabrication of Ultrathin Porous Nickel Hydroxide-Manganese Dioxide Hybrid Nanosheets for Supercapacitor Electrodes with Excellent Capacitive Performance. *Advanced Energy Materials* **2013,** 3, 1636-1646.
65. Wang, X.; Kajiyama, S.; Iinuma, H.; Hosono, E.; Oro, S.; Moriguchi, I.; Okubo, M.; Yamada, A., Pseudocapacitance of Mxene Nanosheets for High-Power Sodium-Ion Hybrid Capacitors. *Nature Communications* **2015,** 6.
66. Feng, J.; Sun, X.; Wu, C.; Peng, L.; Lin, C.; Hu, S.; Yang, J.; Xie, Y., Metallic Few-Layered Vs2 Ultrathin Nanosheets: High Two-Dimensional Conductivity for in-Plane Supercapacitors. *J Am Chem Soc* **2011,** 133, 17832-17838.
67. Huang, K.-J.; Zhang, J.-Z.; Shi, G.-W.; Liu, Y.-M., Hydrothermal Synthesis of Molybdenum Disulfide Nanosheets as Supercapacitors Electrode Material. *Electrochimica Acta* **2014,** 132, 397-403.
68. Ratha, S.; Rout, C. S., Supercapacitor Electrodes Based on Layered Tungsten Disulfide-Reduced Graphene Oxide Hybrids Synthesized by a Facile Hydrothermal Method. *ACS Applied Materials & Interfaces* **2013,** 5, 11427-11433.
69. Wang, X.; Ding, J.; Yao, S.; Wu, X.; Feng, Q.; Wang, Z.; Geng, B., High Supercapacitor and Adsorption Behaviors of Flower-Like Mos2 Nanostructures. *Journal of Materials Chemistry A* **2014,** 2, 15958-15963.
70. Bissett, M. A.; Kinloch, I. A.; Dryfe, R. A. W., Characterization of Mos2-Graphene Composites for High-Performance Coin Cell Supercapacitors. *ACS Applied Materials & Interfaces* **2015,** 7, 17388-17398.
71. Chen, J.; Sheng, K.; Luo, P.; Li, C.; Shi, G., Graphene Hydrogels Deposited in Nickel Foams for High-Rate Electrochemical Capacitors. *Advanced Materials (Weinheim, Germany)* **2012,** 24, 4569-4573.
72. Higgins, T. M.; Coleman, J. N., Avoiding Resistance Limitations in High-Performance Transparent Supercapacitor Electrodes Based on Large-Area, High-Conductivity Pedot:Pss Films. *ACS Applied Materials & Interfaces* **2015,** 7, 16495-16506.
73. Chmiola, J.; Yushin, G.; Dash, R.; Gogotsi, Y., Effect of Pore Size and Surface Area of Carbide Derived Carbons on Specific Capacitance. *J. Power Sources* **2006,** 158, 765-772.
74. Gholamvand, G.; McAteer, D.; Backes, C.; McEvoy, N.; Harvey, A.; Berner, N. C.; Hanlon, D.; Bradley, C.; Godwin, I.; Rovetta, A.; Lyons, M. E. G.; Duesberg, G. S.; Coleman, J. N., Comparison of Liquid Exfoliated Transition Metal Dichalcogenides Reveals Mose2 to Be the Most Effective Hydrogen Evolution Catalyst. *Nanoscale* **2015,** submitted.
75. De, S.; King, P. J.; Lotya, M.; O'Neill, A.; Doherty, E. M.; Hernandez, Y.; Duesberg, G. S.; Coleman, J. N., Flexible, Transparent, Conducting Films of Randomly Stacked Graphene from Surfactant-Stabilized, Oxide-Free Graphene Dispersions. *Small* **2010,** 6, 458-464.

ToC fig

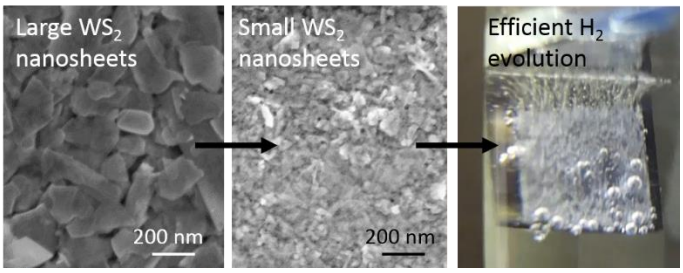
Large WS_2 nanosheets
200 nm
Small WS_2 nanosheets
200 nm
Efficient H_2 evolution